Subsurface Damage and Microstructure Development in Precision Microground Hard Ceramics Using MRF Spots

Introduction

Chemical vapor–deposited (CVD) silicon carbide (Si_4C/SiC), polycrystalline alumina (Al_2O_3/PCA), and aluminum oxynitride ($Al_{23}O_{27}N_5$/ALON) polycrystalline ceramics display a great potential for advanced optical applications in severe environments that require high hardness, high toughness, and excellent thermal properties. These materials are nominally fully dense; therefore, there is growing interest in grinding and ultimately polishing them to nanometer levels of surface microroughness.

Grinding of ceramic materials usually involves the use of metal- or resin-bonded diamond abrasive wheels.[1] The material-removal mechanism can be described by indentation fracture mechanics, where removal is caused by multiple indentation events.[2,3] Two crack systems extend from the plastic deformation zone induced by the indentation: median/radial and lateral cracks.[2] For a given process, lateral cracks control the extent of material removal,[4,5] while the extensions of median/radial cracks are commonly associated with subsurface damage (SSD),[6] which contributes to the degradation of the materials' strength.[2]

For optical applications, SSD can be the source of component instability (e.g., surface stress) and contamination. Polishing abrasives embedded in cracks can lead to laser-induced damage, and thermal cycling can result in component fracture.[7–9] Therefore, determination of SSD depth is critical for high-quality optics. Unfortunately, SSD from grinding is often masked by a deformed surface layer that is smoothed or smeared over the part surface.[9–11] For polycrystalline ceramics, this layer may also consist of pulverized grains or powder. The thickness of this deformed layer varies along the ground surface because of the nonhomogeneity of the composite and the nonuniform distribution of diamond abrasives on the grinding wheel.[12] Therefore, it is valuable to develop new analytical techniques for understanding the damaged surface left from grinding and how it extends into the subsurface for these optical ceramics.[9,10]

Different techniques for estimating SSD depth induced by grinding have been pursued. Randi *et al.*[13] reviewed both nondestructive and destructive techniques to evaluate SSD in brittle materials. Nondestructive methods include transverse electron microscopy, x-ray diffractometry, Raman spectroscopy, optical microscopy, photoluminescence, and the use of ultrasound for ground ceramic materials. Destructive techniques include taper polishing, cleavage, sectioning, ball dimpling, and spotting with magnetorheological finishing (MRF). These destructive techniques are ultimately followed by microscopy or diffractive-based techniques to observe and measure SSD depth.

One recent example of a nondestructive technique is light scattering, as described by Fine *et al.*,[7] whose results were confirmed by the sectioning technique. Another recent study by Wang *et al.*[8] showed how the measurement of the quasi-Brewster angle (qBAT) as a function of wavelength could be used to estimate SSD depth for polished CaF_2 (111) surfaces. The MRF spot technique, as described by Randi *et al.*,[13] was used by Wang *et al.*[8] to validate their results.

Examples of sectioning techniques include the work by Xu *et al.*[14] done on polycrystalline alumina scratched by a single diamond, or Kanematsu,[10] who visualized the morphology of SSD induced by grinding on silicon nitride. His approach included a combination of taper-polishing and plasma-etching techniques, finally observing SSD using scanning electron microscopy (SEM). In addition, dye impregnation was used to identify the crack morphology of previously ground samples that were subsequently broken using a flexure test.[10] Miller *et al.*[9] and Menapace *et al.*[5,15] utilized MRF computer numerically controlled (CNC) machines with raster polishing capabilities to study the distribution of SSD in larger, polished fused-silica parts by fabricating a wedge.

SSD depth can also be estimated by correlating SSD depth to the grinding-induced surface microroughness, or by correlating SSD depth to the size of grinding or polishing abrasives. Preston[16] showed that surface microroughness was three to four

times the SSD depth, by comparing polished and ground glass microscope slides in the early 1920s. In the 1950s Aleinikov[17] expressed the proportionality factor to be ~4 for optical glasses and ceramics. Hed *et al.*[18] extended Aleinikov's work using bound-abrasive tools (diamond and boron carbide), finding that the ratio between SSD depth and peak-to-valley (p–v) surface microroughness (measured using a contact profilometer) for Zerodur, fused silica, and BK-7 glass was ~6.5, a much higher value than previous results. For a large variety of optical glasses ground with bound-abrasive diamond tools, Lambropoulos *et al.*[19] estimated SSD depth to be less than two times the p–v surface microroughness (from areal measurements using a white-light interferometer). In more recent work, Randi *et al.*[13] found the ratio between p–v microroughness (from areal measurements using a white-light interferometer) and SSD to be 1.4 for some optical single crystals ground with diamond-bonded tools, where SSD was measured directly by combining MRF spotting and microscopy techniques. Using the MRF-based technique described here, we demonstrated that, for nonmagnetic nickel-based tungsten carbides (WC-Ni—a challenging composite for optical applications), there is a strong positive correlation between p–v surface microroughness (from areal measurements using a white-light interferometer) and SSD depth for rough-ground surfaces.[20] The application of this technique to magnetic cobalt-based tungsten carbides (WC-Co) was also successful.[21] In all work cited above, it is critical to be aware of the instruments used to characterize surface roughness since different instruments produce different surface-roughness values, due to their different lateral scale-length capabilities.

SSD was also found to be a function of abrasive size used in the controlled grinding stages for fabrication of precision optics, as discussed by Lambropoulos[22] for a variety of optical glasses and glass ceramics. In practice, by reducing the abrasive size with each grinding cycle, the plastically deformed material is removed, reducing the residual stresses associated with the indentation events, and subsequently reducing the initiation of cracks within the plastic zone.[4] This suggests that, by gradually reducing abrasive size, SSD can be minimized with every subsequent grinding step.

We present here a procedure for estimating SSD depth induced by deterministic microgrinding of hard polycrystalline optical ceramics with diamond-bonded tools. This estimate comes from tracking the evolution of surface microroughness (measured using a white-light interferometer) with the amount of material removed by multiple MRF spots (measured using a contact profilometer) of increasing depth into the surface. In addition to extending our p–v microroughness/SSD correlation to hard ceramics, this technique also reveals information about the specimen microstructure (i.e., grain size), mechanical properties (i.e., hardness and fracture toughness), and the grinding conditions (i.e., abrasive size used), from extended spotting with the MRF process.

Experimental Procedure

1. Materials

Samples were obtained from the following sources: three ALON (Surmet Corp., MA, Lot 1472, April 2006) disks (40 mm in diameter × 15 mm thick), two PCA (commercial manufacturer) disks (40 mm in diameter × 2.5 mm thick), and three CVD SiC (Rohm and Haas Company, Advanced Materials, MA) disks (76 mm in diameter × 11.5 mm thick). Grain-size ranges were 150 to 250 μm for ALON, submicron size for PCA, and 5 to 10 μm for CVD SiC.

2. Mechanical Properties (Hardness and Fracture Toughness)

Hardness measurements were taken on a Tukon microindenter equipped with a Vickers diamond indenter and a built-in microscope (×50 objective). A constant dwell time of 15 s was used, with a nominal indentation load of 1 kgf (9.8 N). Averaging was performed on the diagonals of five to ten random indents on the surface.

In the case of ALON, individual grains were easily distinguished, allowing placement of indentations in the middle of individual grains. There were no grain boundaries observable for CVD SiC and PCA using the microscope. For all of the materials tested, indentations were randomly placed on specimen surfaces, avoiding large pores and/or inclusions.

Fracture toughness K_c values were calculated from the observed radial cracks produced at the indentation corners using the Evans correlation.[23] The relevant physical and mechanical properties are listed in Table 110.IV.

3. Grinding Experiments

All samples were processed under the same conditions using deterministic microgrinding. The first set of grinding experiments was performed on a CNC grinding machine[25] using a contour-tool grinding configuration for flat surfaces [see Fig. 110.34(a)], with three different diamond tools: rough, medium, and fine (40-μm, 10- to 20-μm, and 2- to 4-μm grit size, respectively). Both the rough and medium tools had a bronze matrix while the fine tool matrix was resin. To avoid tak-

ing the part off the machine between operations, the tools were trued and dressed in advance using Al_2O_3 dressing sticks that were 320 or 800 grit (29- to 32-μm and 9- to 12-μm grit size, respectively). Table 110.V lists the grinding conditions used.

For PCA an additional grinding experiment was performed because of the large form error on the part surface from grinding using the previous contour configuration. These experiments were completed on a CNC grinding machine[26] using a ring-tool grinding configuration for flat surfaces [see Fig. 110.34(b)]. Grinding was done using rough and medium diamond tools (65-μm and 10- to 20-μm grit size, respectively). Both tools had a bronze matrix, and dressing procedures were performed as discussed above. Table 110.V lists the grinding conditions used.

Table 110.IV: Physical and mechanical properties of hard ceramics listed by increasing Vickers hardness and fracture toughness.[(a)]

Material ID	Density ρ (g/cm^3)	Grain size (μm)	Young's modulus E (GPa)	Vickers hardness H_V (GPa)	Fracture toughness K_c $\left(\text{MPa}\sqrt{m}\right)$[(b)]
ALON ($Al_{23}O_{27}N_5$)	3.69[(c)]	150 to 250	334	15.4±0.3[(d)]	2.7±0.2
PCA (Al_2O_3)	3.99[(e)]	<1	400[(f)]	21.6±0.3[(g)]	3.3±0.1
CVD SiC (Si_4C)	3.21	5 to 10	466	25.0±0.1[(g)]	5.1±0.3

(a) Catalog values, unless otherwise specified.
(b) Calculated using the Evans correlation.[23]
(c) Density may vary slightly depending on the stoichiometry.
(d) Averaging ten Vickers indentations at 1 kgf.
(e) Using Archimedes' water immersion principles.[24]
(f) Calculated from measurement using ultrasonic tests and density values. Data were averaged for two PCA disks (~30 mm in diameter × ~1 mm thick) polished on both sides.
(g) Averaging five Vickers indentations at 1 kgf.

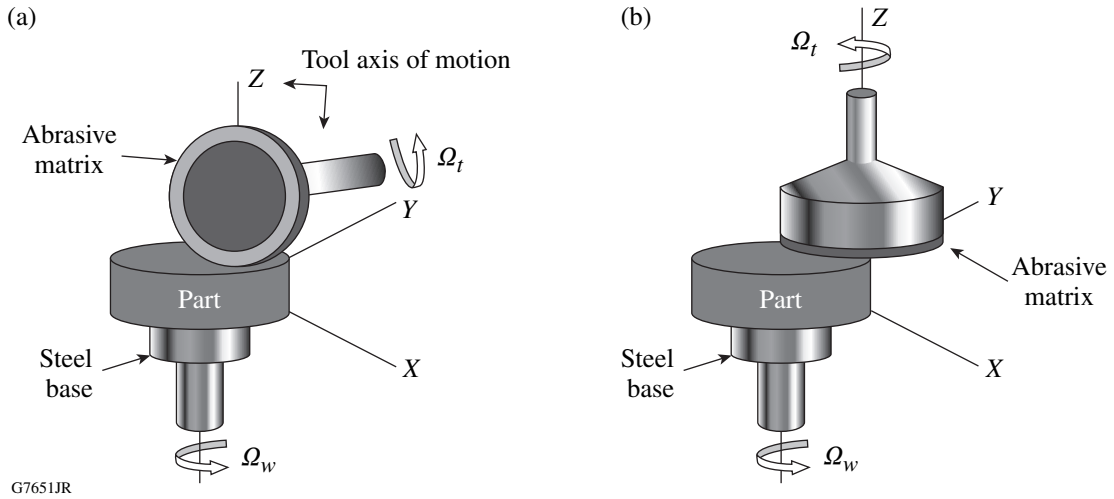

Figure 110.34
Schematics of the two grinding configurations used in our experiments: (a) contour and (b) ring-tool configurations.

Table 110.V: Grinding conditions used in a single pass.[a]

Tool grit size (μm)	Depth of cut (μm)	In-feed (z axis) (mm/min)	Duration of single pass	Cross-feed (x axis) (mm/min)	Duration of single pass (min)
Contour tool grinding configuration.[25]					
40[b]	100	0.5	12 (s)	1.0	30 to 40
10 to 20[b]	20	0.5	2.4 (s)	1.0	30 to 40
2 to 4[c]	5	0.5	0.6 (s)	5.0	6 to 8
Ring tool grinding configuration.[26]					
65[b]	100	0.1	~20 (min)	NA	NA
10 to 20[b]	30	0.01	~45 (min)	NA	NA

[a] The following parameters remained constant: Wheel speed, Ω_t = 6800 rpm for contour tool grinding; Ω_t = 3000 rpm for ring tool grinding; work spindle speed, Ω_w = 100 rpm in both cases.
[b] Bronze bonded, 75 diamond concentration.
[c] Resin bonded, 75 diamond concentration.

Before all grinding experiments, each workpiece was attached to a steel base with hot wax and then placed in the grinding machine parallel to the tool axis of rotation. Water–oil emulsion coolant[27] was delivered to the tool/workpiece interface to avoid burnout and thermal damage. In the case of the contour grinding configuration, grinding was done with two passes for each tool; i.e., the total material removed per tool was 200, 40, and 10 μm (rough, medium, and fine tools, respectively). No subsequent "spark-out " passes were performed. For example, the fine grinding was done only after the part had gone through two-pass cycles with the rough and medium tools. Finally, the workpieces were cleaned using acetone. For ring-tool grinding, multiple tool passes were performed until material was evenly removed from the surface.

4. Spotting of Ground Surfaces

Magnetorheological finishing (MRF)[28,29] is a commercial polishing process for the manufacturing of precision optics. We used MRF spotting, with a commercial CNC machine,[30] in our experiment to estimate the depth of subsurface damage induced by grinding. For all of our experiments, MRF spots were polished onto the ground surface of a nonrotating part, by lowering the part surface into contact with a rotating magnetic fluid ribbon. The MRF fluid used was a commercial product[31] that consisted of an aqueous mixture of nonmagnetic nanodiamond abrasives, magnetic carbonyl iron, water, and stabilizers. Machine parameters such as the magnetic-field strength (~2 to 3 kG), wheel speed (250 rpm), pump speed (125 rpm), ribbon height (1.6 mm), and depth of the part penetrating into the ribbon (0.3 mm) were kept constant and the spotting time was varied. Spotting was done on previously rough-ground, medium-ground, and fine-ground surfaces of each material. Multiple spots with time durations of 1 to 8, 12, and 16 min were taken on subsets of the ground surfaces of ALON and CVD SiC, whereas in the case of the PCA, multiple spots with time durations of 6, 12, 24, 48, and 96 min were taken as described in **Surface Evaluation from the Spotting Experiments** (p. 103).

5. Microscopy of Processed Surfaces

Surfaces were studied using a contact profilometer, a white-light interferometer, a scanning electron microscope (SEM), and an atomic force microscope (AFM). Before the surfaces were analyzed, the samples were ultrasonically cleaned in acetone (30 min at room temperature), then rinsed with alcohol, and finally dried using a nitrogen gun.

Metrology was conducted as follows:

- A stylus profilometer[32] was used to perform 3-D scans of the MRF spots, which were then used to extract the spots' physical dimensions, i.e., spot volume, peak removal depth, and spot profile. The stylus tip is a cone with a 60° angle and a 2-μm spherical tip radius of curvature. The instrument has a 12-nm vertical resolution, and the lateral resolution is about the size of the tip.

- Average microroughness data [peak-to-valley (p–v) and root mean square (rms)] were obtained with a noncontacting white-light interferometer[33] over five 350 × 250-μm^2 areas

randomly distributed across ground areas and within MRF spots as described in **Surface Evaluation from the Spotting Experiments** (p. 103). This instrument has a lateral resolution of ~1 μm and a vertical resolution of ~0.3 nm. The motorized XY stage and field-of-view stitching software allow this instrument to be programmed to measure a large area at high resolution.

- The morphologies of the processed surfaces following grinding, and for selected MRF spots, were analyzed using a field emission SEM.[34] The preferred imaging configuration was a mix signal of the in-lens and in-chamber secondary electron detectors. Surfaces of ground and spotted CVD SiC material were not etched or coated prior to SEM. Imaging of the nonconductive materials (i.e., PCA and ALON) was also performed without etching or application of a conductive coating, using a low beam voltage (1.5 to 0.7 kV), at an ~3-mm working distance.

- Additional surface scans for selected spots were taken on the AFM[35] over three 10×10-μm^2 areas randomly distributed within spots where the deepest point of fluid penetration (ddp) occurred, as discussed in **Surface Evaluation from the Spotting Experiments** (p. 103). Silicon tips with tip radii of approximately 10 nm were used. The lateral image resolution can be as small as the tip radius (5 to 15 nm) and the instrument vertical noise resolution is less than 0.5 Å.

Experimental Results

1. Surface Microroughness and Surface Morphology from Grinding

Surface microroughness data for all materials after each grinding stage were taken using the white-light interferometer. As expected, surface microroughness decreased with decreasing diamond abrasive size. Using the light microscope[36] we observed pitting on the ground surfaces, with no traces of grain boundaries for all the materials tested, as seen in Fig. 110.35. The p–v surface microroughness varied from ~14.5 μm (ALON) to ~3.7 μm [CVD SiC; see Fig. 110.35(a)] after grinding with the rough tool (40-μm grit size), from ~12 μm (ALON) to ~3.5 μm (CVD SiC) for the medium tool (10- to 20-μm grit size), and from ~4 μm [ALON; see Fig. 110.35(b)] to ~0.4 μm [CVD SiC; see Fig. 110.35(c)] for the fine tool (2- to 4-μm grit size). Surface microroughness for PCA was ~9 μm [see Fig. 110.35(d)] with the medium ring tool (10- to 20-μm grit size).

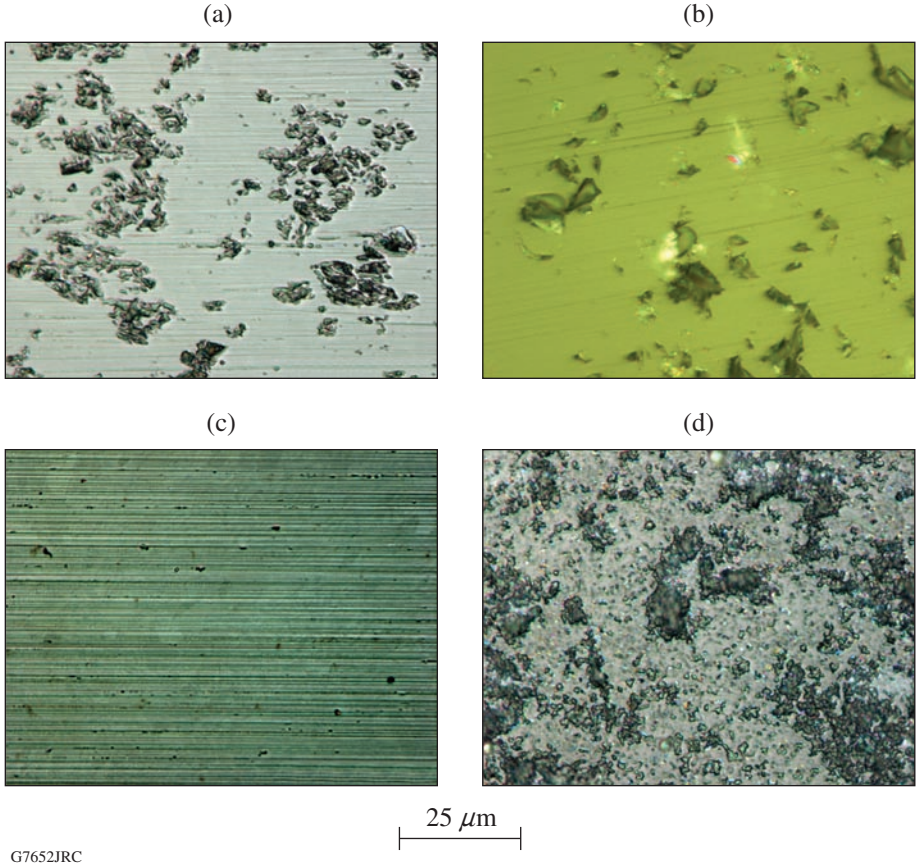

Figure 110.35
Light microscope images of ground surfaces: (a) rough-ground CVD SiC (5- to 10-μm grain size, 40-μm tool grit size with contour configuration, ~4-μm p–v); (b) fine-ground ALON (150- to 300-μm grain size, 2- to 4-μm tool grit size with contour configuration, ~4-μm p–v); (c) fine-ground CVD SiC (5- to 10-μm grain size, 2- to 4-μm tool grit size with contour configuration, ~0.4-μm p–v); (d) medium-ground PCA (submicron grain size, 10- to 20-μm tool grit size with ring configuration, ~8.5-μm p–v).

By using the SEM's high-magnification capabilities we examined the morphologies of the ground surfaces with greater detail. Figure 110.36(a) shows the morphology of the rough-ground ALON, where the material microstructures, i.e., grain boundaries, are not visible. By using high magnification, Fig. 110.36(b) shows that the removal mechanism involved fracture. Figure 110.36(c) shows that for CVD SiC, the rough-ground surface is pitted, with the surrounding surface relatively smooth. Using higher magnification, Fig. 110.36(d) shows that the pit lengths, approximately 5 μm long, are comparable to the average grain size (5 to 10 μm) of this CVD SiC material.

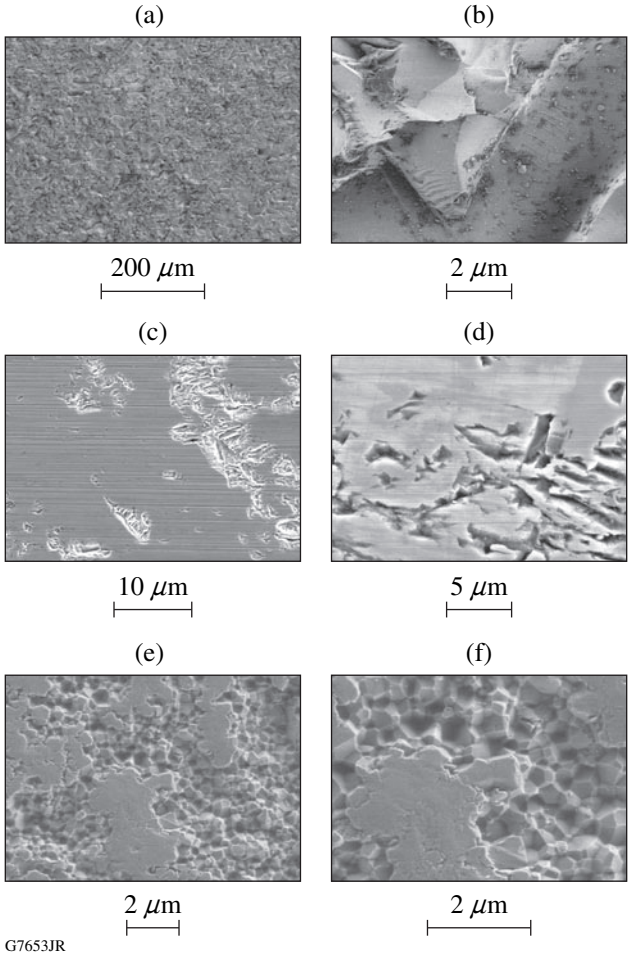

Figure 110.36
Morphology of the as-ground surfaces using SEM with different magnifications: (a),(b) ALON ground with contour configuration, 40-μm tool grit size, and ~14.5-μm p–v, low and high magnification, respectively, taken using low beam voltage (1 kV), at a 5-mm working distance; (c),(d) CVD SiC ground with contour configuration, 40-μm tool grit size, ~4-μm p–v, low and high magnification, respectively, taken using nominal beam voltage (10 kV), at a 10-mm working distance; and (e),(f) PCA ground with ring configuration, 10- to 20-μm tool grit size, ~8.5-μm p–v, low and high magnification, respectively, taken using low beam voltage (1.5 kV), at a 3-mm working distance.

Examination of the PCA surface in Fig. 110.36(e) shows that the deformed layer induced by grinding covers/masks the grains and any SSD, for PCA. Using higher magnification, Fig. 110.36(f) shows the exposed PCA subsurface where it appears that single grains pulled out, leaving craters of the order of 0.2 to 0.4 μm wide.

2. Surface Evaluation from the Spotting Experiments

MRF spots of increasing time duration were taken on all ground surfaces. Figure 110.37(a) shows a typical 3-D map generated with a profilometer for an 8-min MRF polishing spot taken on a rough-ground CVD SiC surface. After using the software to remove form figure errors (e.g., tilt and curvature), we calculated the physical properties such as volume and maximum amount of material removed by the MRF spot (i.e., spot depth). The volumetric removal rates for ALON, CVD SiC, and PCA using the MRF operating conditions described previously were found to be 0.020, 0.006, and 0.002 mm^3/min, respectively, from averaging the results of four spots.

The area enclosed by the white ellipse in Fig. 110.37(a) constitutes the region of maximum removal within the spot, where the depth of deepest penetration (ddp) into the subsurface

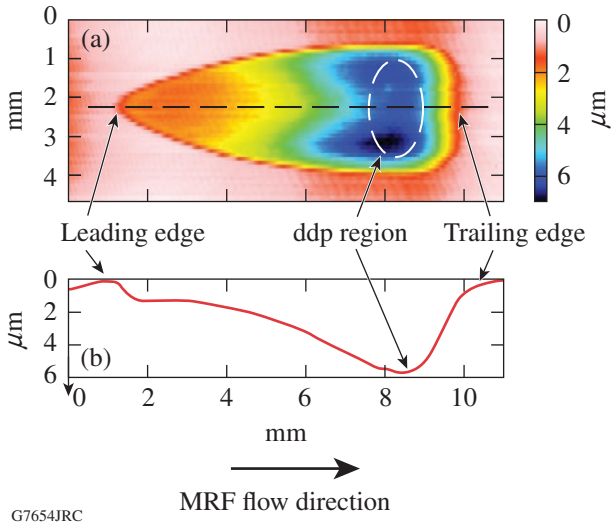

Figure 110.37
(a) 3-D image of an MRF spot taken with a contact stylus profilometer on rough-ground CVD SiC for 8 min. Arrows indicate the spot's leading edge (where an MRF ribbon first contacts the material), the spot's ddp region, identified by an ellipse (deepest point of part penetration into the MRF fluid ribbon), and the spot's trailing edge. The fluid flow direction is from left to right. (b) Spot profile extracted from a line scan through the center of the 3-D map (indicated by a dashed line). The distance between the trailing edge and the ddp region is ~2 mm in the horizontal direction. The spot depth reaches ~6 μm in the region sampled with the line scan.

occurs. The ddp in Fig. 110.37(a) has some asymmetry with respect to the spot center profile line [shown in Fig. 110.37(b)], in this case exhibiting a variation of ±0.6 μm. This feature is typically encountered for many of the longer-time-duration spots examined in this work. It could be due, in part, to subtle misalignments of the plane of a part surface with respect to the MRF ribbon. Figure 110.37(b) illustrates how we extract the spot center profile from the 3-D map to establish the location of the ddp region relative to the trailing edge for roughness measurements.

Figure 110.38(a) shows a 3-D map of a different spot taken on a rough-ground CVD SiC surface transverse to the MRF flow direction (as indicated by an arrow in the figure), with the white-light interferometer in stitching mode. Figures 110.38(b) and 110.38(c) give 3-D maps (0.3 × 0.3 mm^2) of the rough-ground surface and within the ddp, extracted from the map of Fig. 110.38(a), respectively. Figures 110.38(d) and 110.38(e) show line scans, or 2-D profiles, extracted from Figs. 110.38(b) and 110.38(c) (as indicated by the arrows), respectively. These line scans show the significant roughness reduction from ~1.4-μm p–v [~100-nm rms; Fig. 110.38(d)] for the ground surface to ~95-nm p–v [~18-nm rms; Fig. 110.38(e)] achieved inside the MRF spot, in agreement with the areal microroughness values, which vary from ~3.2-μm p–v [~99-nm rms; Fig. 110.38(b)] on the ground surface and ~170-nm p–v [~19-nm rms; Fig. 110.38(c)] within the spot ddp. Note that the discrepancy between the line scans and the areal data

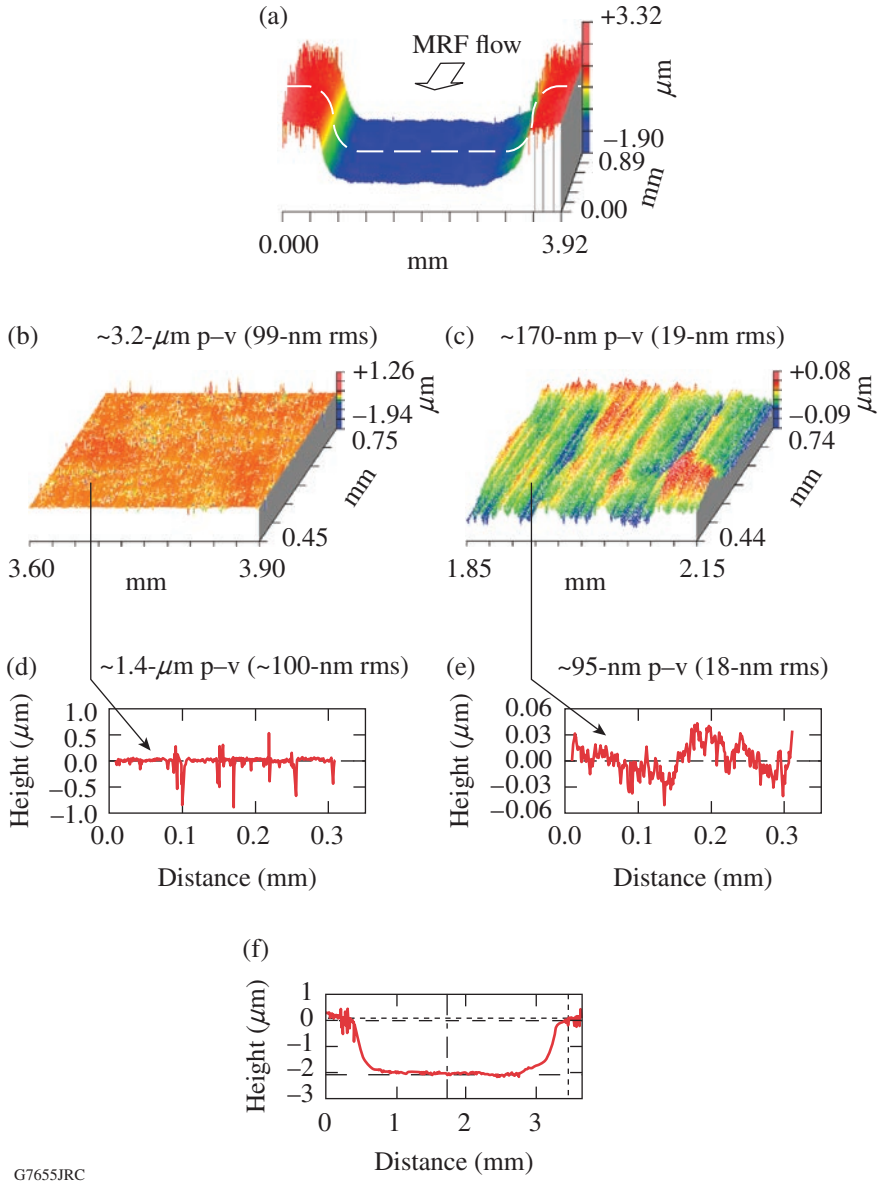

Figure 110.38
Scans taken on rough-ground CVD SiC, spotted for 3 min: (a) 3-D map done with the white-light interferometer in stitching mode, transverse to the MRF flow (see arrow indicating the MRF flow direction); (b),(c) areal maps (0.3 × 0.3 mm^2) of microroughness on the ground surface and within the spot ddp, respectively; (d) line scan of the ground surface, taken from the center of (b); (e) line scans within the ddp region transverse to the MRF flow direction, taken from the center of (c) (as indicated by the arrows); and (f) line scan of the spot-width profile (indicated by a dashed white line in the 3-D map) in (a).

comes from the larger areas sampled with the latter method. Another discrepancy between the 3-D map and line scans in Fig. 110.38 is associated with the spot depth. The vertical scale in Fig. 110.38(a) indicates the overall areal p–v roughness variations of ~5.2 μm, which artificially indicates a spot depth of that scale because it includes the highest peaks on the rough surface. However, when we examine single line scans of the spot width profile [represented by a dashed line in Fig. 110.38(a)], the spot depth is shown to be ~2 μm [see Fig. 110.38(f)].

After the location of a given spot's ddp was identified [as described in Fig. 110.37(b)], areal surface microroughness measurements were taken using the white-light interferometer at five random locations within the ddp region over areas of 0.35×0.26 mm^2 as seen schematically in Fig. 110.39(a). In addition, horizontal line scans were taken perpendicular (⊥) to the MRF flow direction. Then, the part was rotated by 90° and remeasured so that horizontal line scans parallel (∥) to the MRF flow direction were also obtained, as seen in Fig. 110.39(b). This procedure is necessary because the interferometer analog camera creates images with a horizontal raster pattern.

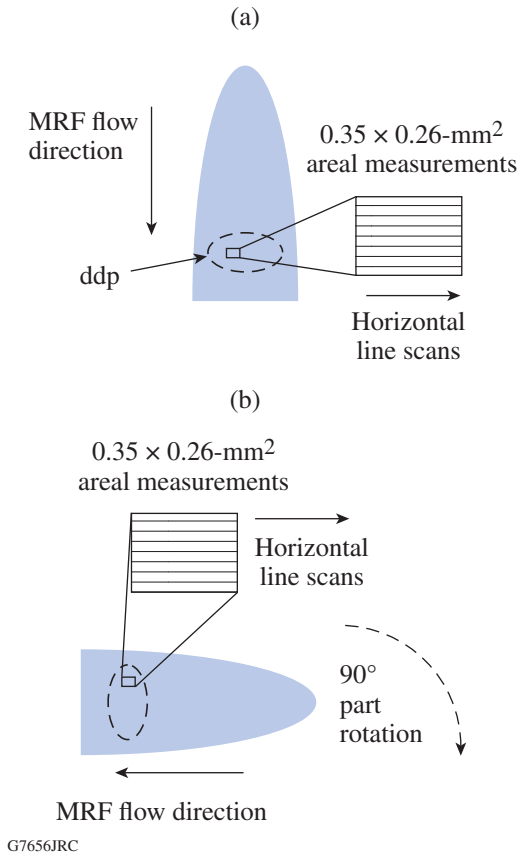

Figure 110.39
Schematic diagram of the procedure used for surface microroughness measurements within MRF spots. The dashed ellipse represents the ddp region. The rectangle within the ddp represents one of five random sites over which surface roughness was measured. (a) First orientation of the spot for generating line scans perpendicular (⊥) to the MR fluid flow direction, and (b) after rotating the part 90° to generate line scans parallel (∥) to the MR fluid flow direction.

Surface microroughness data taken on initial ground surfaces and in ddp areas for long-time-duration spots are listed in Tables 110.VI(a)–110.VI(c). The areal data represent averages of 5 random measurements, while the values for the line scans (⊥ and ∥) represent averages of 50 line scans. The amount of material removed in each spot, or the spot maximum depth, is reported for measurements done using the contact profilometer, as described in the text that discusses Fig. 110.37(a).

Tables 110.VI(a)–110.VI(c) summarize the results of grinding and spotting experiments (the complete set of experimental data can be found elsewhere[37]). The evolution of microroughness with the amount of material removed by the MRF spot indicates that by removing an optimal amount of material from the as-ground surface, p–v surface microroughness was significantly reduced. This observation is valid for all initial surface conditions: rough, medium, and fine ground. For example, in the case of ALON, the initial surface microroughness values were ~14.5-μm p–v (~1.5-μm rms), while after removing ~11 μm with the MRF process, surface microroughness decreased to ~1.2-μm p–v (~0.09-μm rms). When an additional ~13 μm of material were removed, surface microroughness decreased to ~1.1 μm (~0.07-μm rms). In addition, we found differences in microroughness values between areal and line scans, either in a direction perpendicular (⊥) or parallel (∥) to the MRF flow. For example, in the case of CVD SiC, the initial rough-ground surface microroughness values were ~3.7-μm p–v (~0.11-μm rms), whereas using line scans, surface microroughness values were ~1.5-μm p–v (~0.1-μm rms). [Note that there is no preferred directionality to the ground surface.] After removing ~1.7 μm with the MRF process, surface microroughness decreased to ~0.11-μm p–v (~0.02-μm rms) in a direction perpendicular (⊥) to the flow, compared to ~0.06-μm p–v (~0.01-μm rms) measured parallel (∥) to the flow direction. Similar observations can be made in the case of PCA.

Discussion

In this work MRF spots were placed on previously ground hard optical ceramics, exposing the subsurface without introducing new damage. By removing several microns of material (proportional to the initial p–v microroughness in the as-ground state), surface roughness was significantly reduced. With the

removal of additional material (i.e., using longer MRF spotting time), we observed that roughness continued to decrease or to slightly increase.

These results suggest that, after examining the evolution of surface roughness within the spots as a function of the amount of material removed (see Fig. 110.40), two stages can be identified: a stage where removal of the initial grinding damage occurs, and a stage where removal shows the development of a texture relating to the interaction between MRF and the material surface. In the first stage, surface roughness resulting from deformation and fracture by grinding is removed, starting with the initial surface condition and ending when the surface roughness reaches a low value after spotting with MRF. Here the improvement in surface condition is best characterized by the drop in areal p–v roughness, a measurement that captures all features over a reasonably large area.

As seen in Fig. 110.40, the areal p–v for the initially rough-ground ALON [Fig. 110.40(a)], rough-ground CVD SiC [Fig. 110.40(b)], and medium-ground PCA [Fig. 110.40(c)] falls from ~14.5, ~3.7, and ~9 μm to ~1.2, ~0.20, and ~0.25 μm, with ~11, ~1.7, and ~9 μm removed in the first stage, respectively. Beyond this point, differences become apparent in the second stage, depending on how the surface roughness is examined.

Table 110.VI(a): Selected summary of results for grinding and spotting experiments. Surface microroughness measurements were taken at five random locations within a spot ddp with the white-light interferometer. The amount of material removed by MRF (spot maximum depth) was extracted from the 3-D profilometer scans.

Material	**ALON Processed with Contour Tool**			
	Rough ground			
MRF Material Removal (μm)		0 (as ground)	10.93±0.23	23.83±0.12
Areal (μm)	p–v	14.52±1.04	1.2±0.4	1.1±0.2
	rms	1.45±0.02	0.09±0.01	0.07±0.02
Perpendicular (⊥) (μm)	p–v	8.12±0.49	0.40±0.04	0.30±0.06
	rms	1.41±0.05	0.09±0.00	0.07±0.02
Parallel (∥) (μm)	p–v	8.12±0.49	0.39±0.05	0.23±0.10
	rms	1.41±0.05	0.07±0.02	0.06±0.03
	Medium Ground			
MRF Material Removal (μm)		0 (as ground)	9.12±0.11	21.57±0.51
Areal (μm)	p–v	11.72±0.00	0.56±0.16	0.65±0.17
	rms	0.72±0.02	0.09±0.02	0.12±0.03
Perpendicular (⊥) (μm)	p–v	4.84±0.42	0.39±0.09	0.47±0.11
	rms	0.70±0.03	0.09±0.02	0.12±0.03
Parallel (∥) (μm)	p–v	4.84±0.42	0.23±0.06	0.18±0.03
	rms	0.70±0.03	0.05±0.01	0.04±0.01
	Fine Ground			
MRF Material Removal (μm)		0 (as ground)	5.98±0.31	21.50±0.10
Areal (μm)	p–v	4.24±1.44	0.51±0.09	1.05±0.06
	rms	0.10±0.05	0.08±0.01	0.16±0.04
Perpendicular (⊥) (μm)	p–v	0.67±0.50	0.33±0.03	0.72±0.16
	rms	0.07±0.03	0.07±0.00	0.16±0.04
Parallel (∥) (μm)	p–v	0.67±0.50	0.22±0.04	0.19±0.09
	rms	0.07±0.03	0.05±0.01	0.05±0.03

Table 110.VI(b): Selected summary of results for grinding and spotting experiments. Surface microroughness measurements were taken at five random locations within a spot ddp with the white-light interferometer. The amount of material removed by MRF (spot maximum depth) was extracted from the 3-D profilometer scans.

Material	**CVD SiC Processed with Contour Tool**			
	Rough Ground			
MRF Material Removal (μm)		0 (as ground)	1.70±0.060	9.41±0.012
Areal (μm)	p–v	3.680±0.228	0.193±0.042	0.126±0.013
	rms	0.108±0.006	0.021±0.004	0.018±0.004
Perpendicular (⊥) (μm)	p–v	1.453±0.200	0.107±0.014	0.080±0.016
	rms	0.10±0.005	0.020±0.004	0.017±0.004
Parallel (∥) (μm)	p–v	1.453±0.200	0.061±0.008	0.056±0.007
	rms	0.10±0.005	0.013±0.002	0.012±0.001
	Medium Ground			
MRF Material Removal (μm)		0 (as ground)	1.61±0.020	8.64±0.03
Areal (μm)	p–v	3.464±0.177	0.169±0.041	0.140±0.025
	rms	0.077±0.009	0.021±0.007	0.020±0.004
Perpendicular (⊥) (μm)	p–v	1.184±0.066	0.105±0.031	0.080±0.039
	rms	0.070±0.004	0.020±0.007	0.030±0.021
Parallel (∥) (μm)	p–v	1.184±0.066	0.054±0.010	0.047±0.007
	rms	0.070±0.004	0.011±0.002	0.010±0.002
	Fine Ground			
MRF Material Removal (μm)		0 (as ground)	1.86±0.090	10.23±0.120
Areal (μm)	p–v	0.424±0.069	0.141±0.054	0.136±0.025
	rms	0.018±0.002	0.013±0.001	0.019±0.003
Perpendicular (⊥) (μm)	p–v	0.011±0.005	0.073±0.009	0.091±0.012
	rms	0.018±0.001	0.012±0.001	0.019±0.003
Parallel (∥) (μm)	p–v	0.011±0.005	0.060±0.006	0.043±0.006
	rms	0.018±0.001	0.012±0.001	0.009±0.002

Table 110.VI(c): Selected summary of results for grinding and spotting experiments. Surface microroughness measurements were taken at five random locations within a spot ddp with the white-light interferometer. The amount of material removed by MRF (spot maximum depth) was extracted from the 3-D profilometer scans.

Material	**PCA Processed with Ring Tool**			
	Medium Ground			
MRF Material Removal (μm)		0 (as ground)	8.84±0.07	15.9±0.06
Areal (μm)	p–v	8.942±1.067	0.247±0.031	0.276±0.045
	rms	0.569±0.076	0.033±0.006	0.044±0.008
Perpendicular (⊥) (μm)	p–v	3.613±0.401	0.177±0.0028	0.220±0.039
	rms	0.460±0.082	0.033±0.006	0.043±0.008
Parallel (∥) (μm)	p–v	3.613±0.401	0.128±0.008	0.101±0.008
	rms	0.460±0.082	0.030±0.002	0.022±0.002

For orthogonal line scans, the initial ground p–v roughness is similar, as the ground surface shows no processing-related directional features {~8.1-, ~1.4-, ~3.6-μm p–v, for ALON [see Fig. 110.40(a)], CVD SiC [see Fig. 110.40(b)], and PCA [see Fig. 110.40(c)], respectively}. In the case of ALON [Fig. 110.40(a)], for both line-scan orientations (⊥ and ∥) with respect to the direction of MRF fluid flow over the surface, p–v surface roughness is seen to drop from ~400 nm to ~300 (⊥) and ~230 nm (∥), respectively, in the second stage as the diamonds in the MR fluid continue to polish the surface, removing a total of ~24 μm of material. In the case of CVD SiC [Fig. 110.40(b)], p–v surface roughness (⊥) is seen to drop from 107 to 80 nm, whereas p–v surface roughness (∥) drops slightly from 61 to 56 nm, as the diamonds in the MR fluid continue to polish the surface, removing a total of ~9.4 μm of material. In the case of PCA, p–v surface roughness (∥) is seen to drop from ~0.13 to 0.1 μm, as the diamonds in the MR fluid continue to polish the surface, removing a total of 16 μm of material. Although not described here, it is possible to study the microstructure of the material with this sampling technique, one example being decoration of grain boundaries.[38] However, as in the case of PCA [Fig. 110.40(c)], p–v roughness (areal and ⊥) is seen to increase with additional material removed beyond ~9 μm in the second stage. This increase is real, and is due to a texture or grooving impressed on the polished, damage-free surface by the abrasives in the MR fluid. These grooves come from a lack of part rotation during long-duration spotting.

An interesting observation can be made for both ALON and CVD SiC: In the second stage, where the interaction between the MR fluid abrasives and the surface is strong, there is a gradual increase in p–v roughness as shown with all three measurement protocols ending with an abrupt drop in the p–v roughness; after this, the roughness either increases or slightly decreases. For both ALON and CVD SiC, this phenomenon takes place when the amount of material removed by the MRF reaches a depth comparable to the material grain size {~12 and 4 μm for ALON [see Fig. 110.40(a)] and CVD SiC [see Fig. 110.40(b)], respectively}. This phenomenon is not present in the case of PCA [Fig. 110.40(c)], suggesting that, as grain

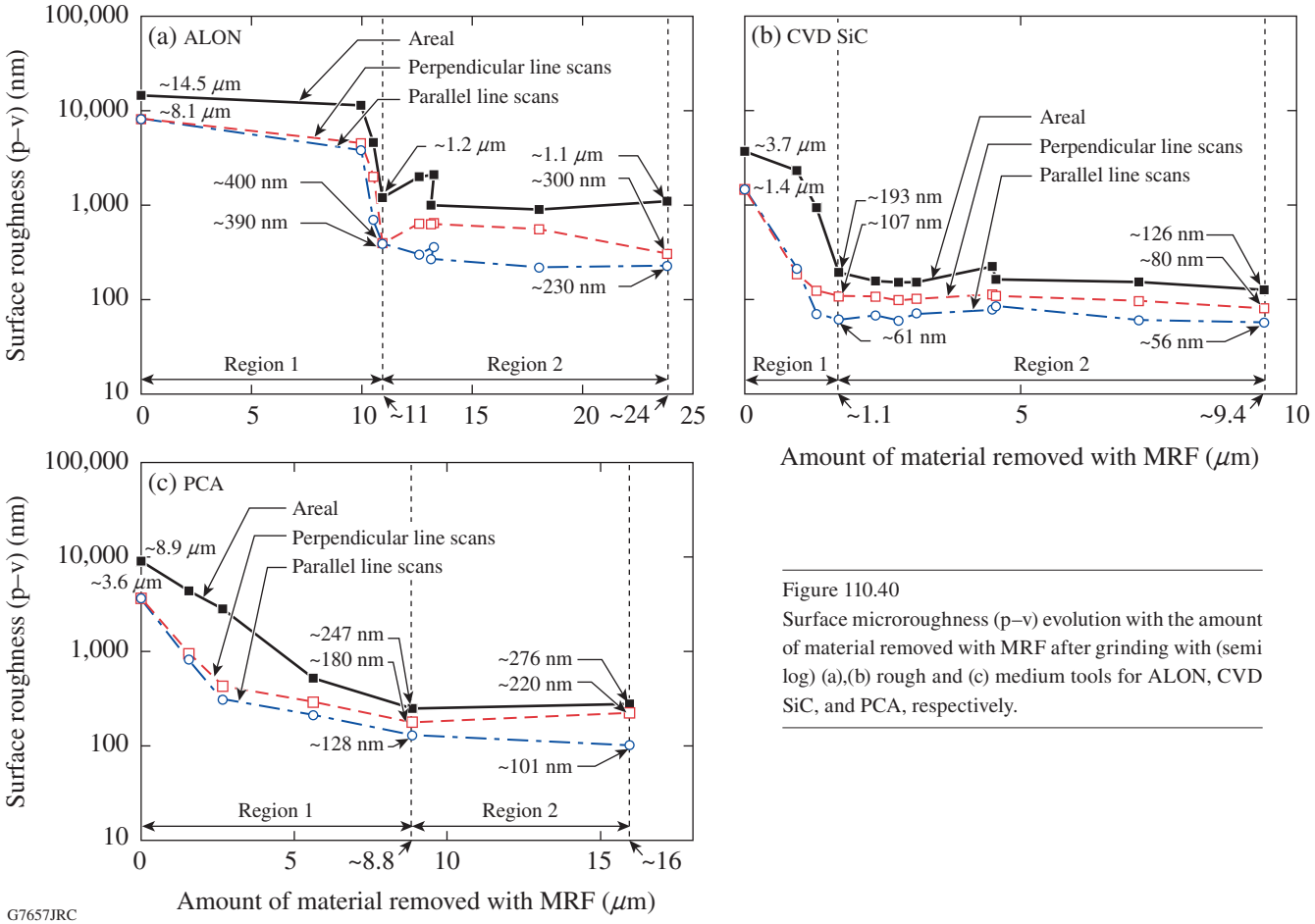

Figure 110.40
Surface microroughness (p–v) evolution with the amount of material removed with MRF after grinding with (semi log) (a),(b) rough and (c) medium tools for ALON, CVD SiC, and PCA, respectively.

size increases, the interaction between a material's grains and the polishing abrasives contributes to surface roughening, or "grain decoration."

SEM analysis within polishing spots confirms that MRF exposes and removes fractured material in both stages 1 and 2, without creating additional damage. Figure 110.41 shows the evolution of surface texture in spots taken on previously medium-ground PCA. Figures 110.41(a) and 110.41(b) represent spot depths of ~2 to 3 μm, where MRF processing exposed voids and pulverized powder regime beneath the deformed layer. Longer spotting times to remove up to a total of 16 μm of material [see Figs. 110.41(c)–110.41(e)] verify that MRF eliminated all pitting and hidden damage, with the subsequent development of a grooved texture.

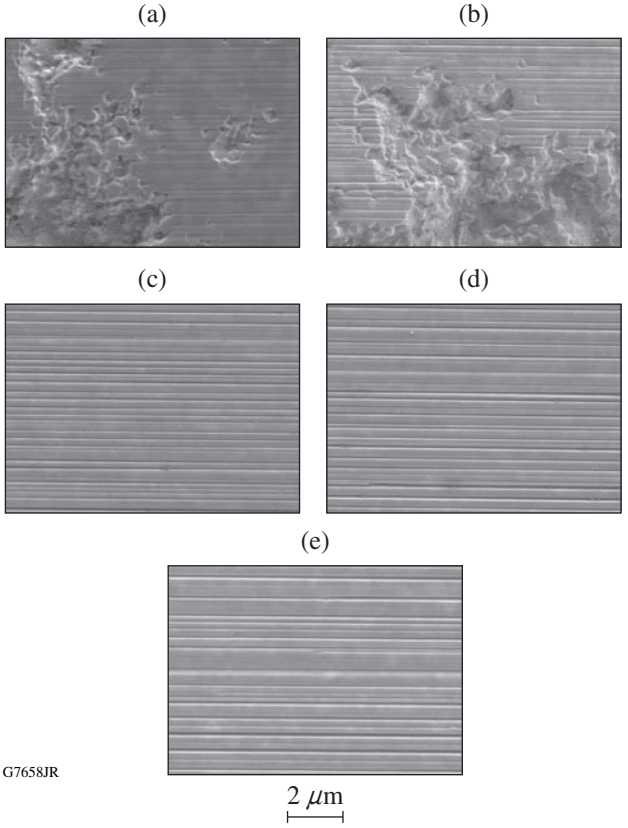

Figure 110.41
SEM images inside MRF spots taken on PCA that was previously medium ground (10- to 20-μm grit size) to an initial roughness of 3.6-μm p–v. (a)–(e) ~1.6-, 2.6-, 5.6-, 9-, and 16-μm spot depths (MRF material removed), respectively. The initial deformation layer as seen in Figs. 110.36(e) and 110.36(f) is completely removed. Long spot dwell times [(d), (e)] enhanced the intrinsic directionality of the MRF process.

1. Use of Power Spectrum to Quantify Surface Topography

In addition to the conventional p–v and rms values that define surface roughness, the interaction between the MR fluid and the material surface is discussed in terms of the power spectral density (PSD). This analysis results in a unique signature,[39] in which surface texture parallel (∥) and perpendicular (⊥) to the MR fluid flow direction may be observed and studied to obtain information on the surface and its microstructure.

For a given surface profile $z(x)$, the rms roughness is defined as

$$\text{rms} = \sqrt{\frac{1}{N} \cdot \sum_{i=1}^{N} z_i^2} \quad (m) \tag{1}$$

and the 1-D PSD at spatial frequency $f_j = j\Delta f$ is[40]

$$PSD_{1\text{-D}}(f_j) \approx \frac{\Delta x}{N}\left|\sum_{k=1}^{N} z_k \exp\left[(2\pi i)jk/N\right]\right|^2, \qquad j = 1,2,\ldots N/2, \tag{2}$$

where $\Delta f = 1/(N\Delta x) = 1/L$, with L being the scan length. PSD is a statistical function that allows a breakdown of the surface roughness over a range of spatial frequencies. Furthermore, the area under a 1-D PSD curve (between two spatial-frequency limits) is a measure of the rms surface roughness in this spatial range:[41]

$$\text{rms}^2_{1\text{-D}} = \int_{f_{\min}}^{f_{\max}} \text{PSD}_{1\text{-D}}(f)\,df. \tag{3}$$

After removing the low-frequency terms (tilt, curvature, etc.) from the roughness data for part surfaces discussed in **Experimental Results** (p. 102), horizontal 1-D PSD plots were generated from areal measurements (0.35×0.26 mm^2) taken with a white-light interferometer over spatial frequencies extending from 2.0×10^{-6} nm^{-1} to 2.0×10^{-2} nm^{-1} by using multiple line scans in a direction perpendicular (⊥) to the MRF flow, as seen in Fig. 110.39(a). Removing the low-frequency terms resulted in an improved PSD spectrum.[42]

Because the white-light interferometer has a lateral resolution limit of 1 μm, additional 1-D PSD plots were generated from AFM scans with a lateral resolution in the nanometer range. These scans were also done within spot ddp regions.

A consideration of PSD data generated from profiles perpendicular (⊥) to the MRF flow direction allows us to study the residual grooving pattern of the MR fluid flow that represents the abrasive/surface interactions.

2. MRF Signature on Hard Materials

Figure 110.42 shows the PSD curves in ddp regions for two spots of increasing time duration taken on the surface of initially rough-ground ALON. The curves represent the evolution of surface texture with the amount of material removed by the MRF spot, from ~10.5 μm to ~24 μm (corresponding to 3- and 16-min spot dwell times, respectively). The interferometer PSD curves (i.e., at lower spatial frequencies) show an amplitude reduction from the short- to the long-dwell-time spots, due to surface smoothing of roughness contributions of the MRF process. The material's microstructure dominates the curve in the spatial frequency range of 7×10^{-5} to 3×10^{-4} nm^{-1}, corresponding to features of the order of ~50 to 100 μm (comparable to the ALON grain size).

AFM measurements were taken and evaluated to examine the PSD across the surface of a single grain in the spatial frequency range of 1×10^{-4} to 1×10^{-2} nm^{-1} (corresponding to features of the order of 10 to 0.1 μm; see scale at top of Fig. 110.42). When compared to the interferometer results, the AFM measurements show a reversal. PSD values for the 16-min-duration spot have higher amplitudes across all relevant spatial frequencies due to the grooving effect of the MRF process on the surface of a single grain. The morphology of the grooving pattern represents the "MRF signature on hard materials." Figures 110.43(a) and 110.43(b) show the surface morphologies within these spots detected by the AFM. Profiles

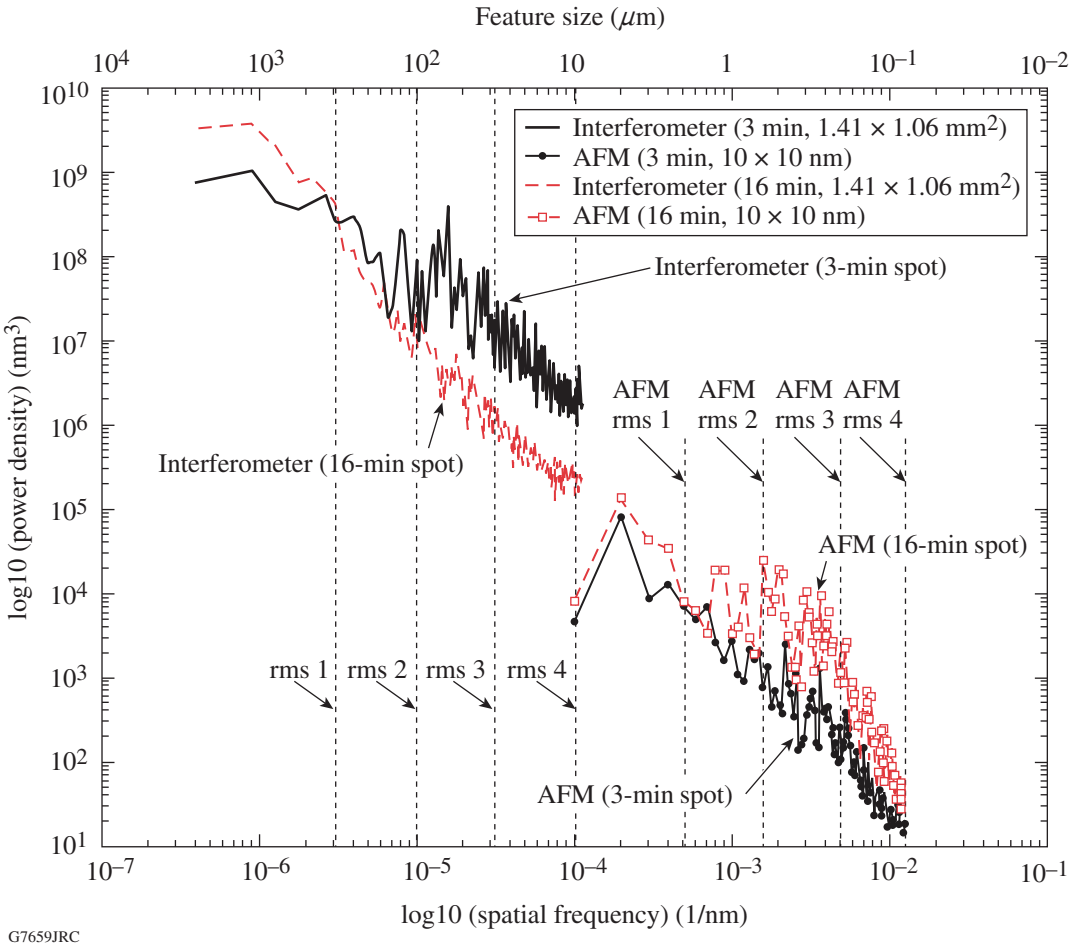

Figure 110.42
PSD (log–log) for MRF spotting done on initially rough-ground (40-μm grit size) ALON. White-light interferometer measurements were taken using a 2.5 objective using a 2× magnification (1.41 × 1.06 mm^2).

of these scans taken across the image diagonal represented by a white line are shown in Fig. 110.43(c) and 110.43(d). The images and accompanying profiles agree well with the PSD function. For example, when we calculate the number of features (~40) across the diagonal (~15 μm) of Fig. 110.43(b), formed by the long-dwell-time MRF spot, the number corresponds to a feature size of the order of 0.5 μm at 2×10^{-3} nm^{-1} spatial frequency, which corresponds to the peak in that frequency, as seen in Fig. 110.42. The markers in Fig. 110.43(c) extend over vertical heights in the range of ~11 to 14 nm, for the short-dwell-time spot, whereas the markers in Fig. 110.43(d) for the long-dwell-time spot extend over vertical heights in the range of ~19 to 30 nm.

The calculated rms values from the PSD curves of Fig. 110.42, designated as rms 1, rms 2, etc., on the figure, are plotted in Fig. 110.44. The left-hand side of Fig. 110.44 shows the calculated rms values for ALON, corresponding to the spatial frequency of the interferometer PSD curves in Fig. 110.42, and the calculated rms values from the PSD curves for CVD SiC and PCA where we used a 20× objective and a ~350-μm spatial scan length (511 data points) in the spatial-frequency range of 0.2×10^{-5} to 0.9×10^{-3} nm^{-1} (corresponding to features of the order of ~100 to 1 μm) on the interferometer. As seen in Fig. 110.42, we notice a decrease in rms surface roughness from the short- to the long-dwell-time spots for ALON (see arrow 1). [The roughness increase for the 16-min spot at low frequencies is due to surface figure errors from grinding.] In the case of CVD SiC there is an increase in the PSD from the short to the long MRF spot dwell time (see arrow 2). This increase represents an increase in surface roughness on the part surface due to decoration of grain boundaries within the spatial-frequency range of 10^{-4} to 10^{-3} nm^{-1}, representing features of the order of 1 to 10 μm, comparable to the material grain size. [The increase in the curve amplitude for CVD SiC (16-min spot) in the low-frequency range is also attributed to surface figure error as mentioned above for ALON.] In the case of PCA, we see a large reduction in roughness values for the long- compared to the short-dwell-time spots (see arrow 3). This can be attributed to surface smoothing of roughness contributions in this interval, in the spatial-frequency range of 3.2×10^{-5} to 10^{-4} nm^{-1}. There is almost no change in the spatial-frequency range of 3.2×10^{-4} to 10^{-3} nm^{-1}, corresponding to a feature size of the order of 3.3 to 1 μm. This represents features that are much larger than the nominal grain size, possibly due to grain clusters.

The right-hand side of Fig. 110.44 shows the calculated rms values for PSD curves done in the spatial-frequency range of 0.0002 to 0.02 nm^{-1} (corresponding to features of the order of 1 to 0.05 μm) using the AFM. These results are within the boundaries of a single grain for ALON, whereas for both CVD SiC (5- to 10-μm grain size) and PCA (submicron-range grain size), these results span at least one grain boundary. Notice

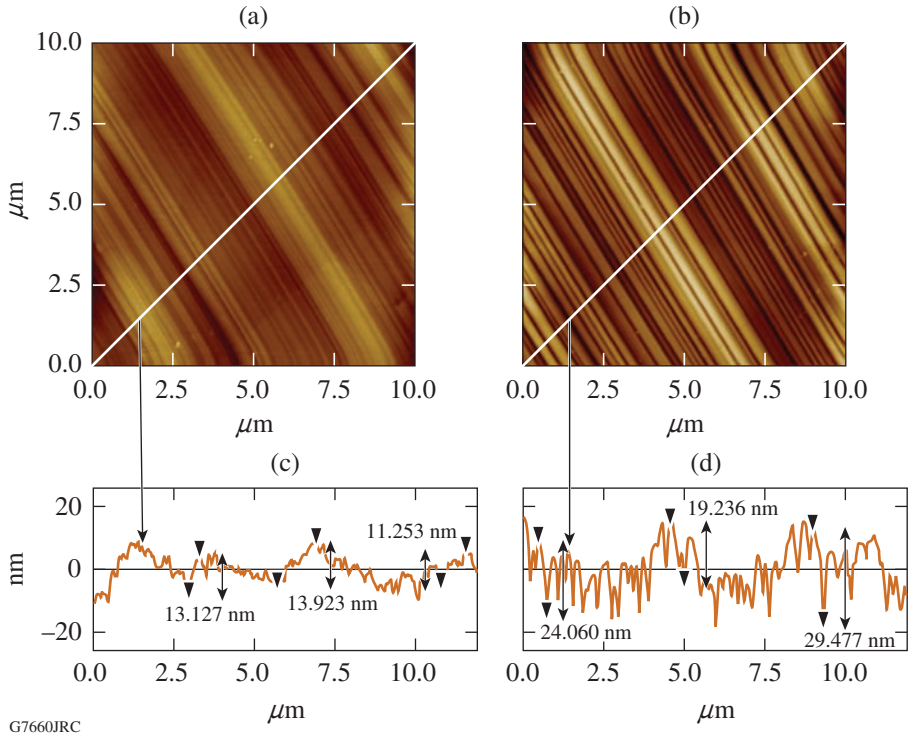

Figure 110.43
AFM scans taken at spots' ddp of initially rough-ground ALON: (a) short- and (b) long-dwell-time spots (3 and 16 min, respectively); (c),(d) profiles taken across the diagonal of scans, represented by the white lines in (a) and (b), respectively. The markers in (c) and (d) represent vertical heights in a range of ~11 to 14 nm and ~19 to 30 nm for the short- and long-dwell-time spot, respectively. The grain size is 50 to 100 μm.

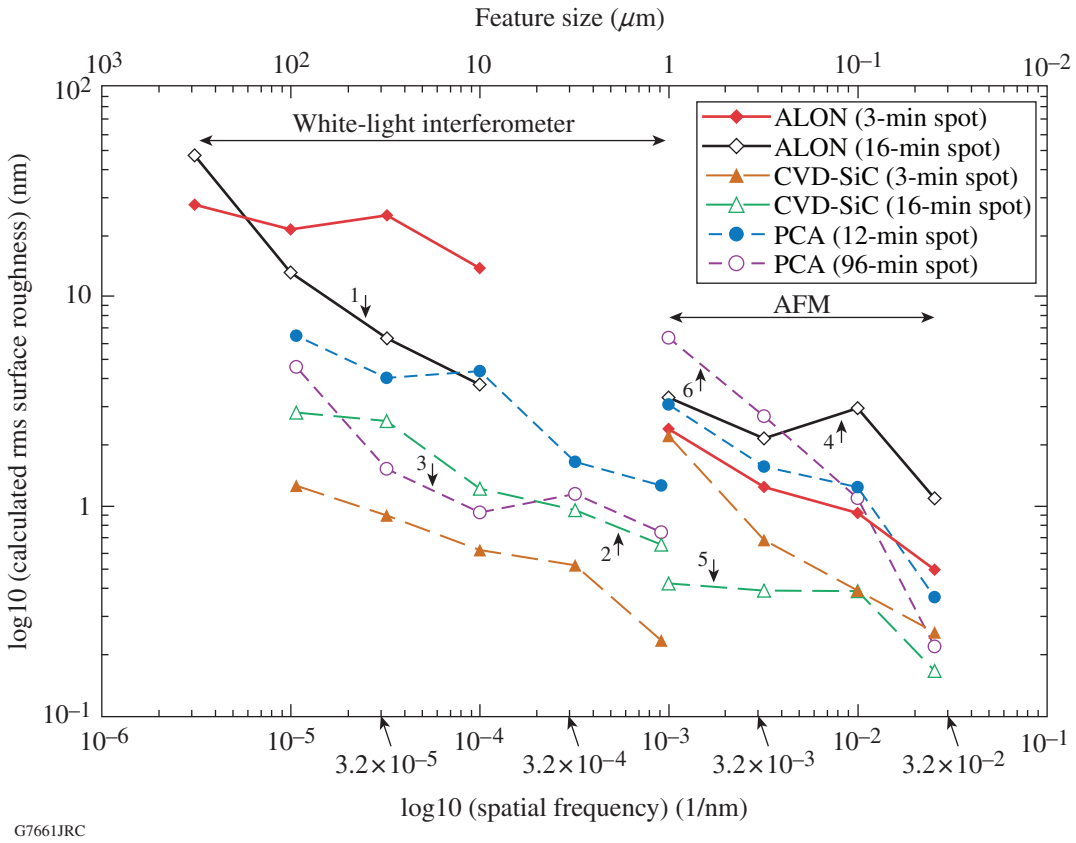

Figure 110.44
Calculated rms (nm) surface roughness from PSD plots generated from the interferometer and AFM measurements (log–log). Data points represent the averaged rms values for a specific spatial-frequency bandwidth, indicated as rms 1, rms 2, etc., in Fig. 110.42.

the increase in the roughness values for ALON at the spatial frequency 10^{-2} nm^{-1} (see arrow 4), indicating the presence of MRF signature, as discussed for Figs. 110.42 and 110.43. There is almost no change in surface roughness at the spatial frequency 10^{-2} nm^{-1} for both CVD SiC and PCA, corresponding to the MRF signature. Beyond this frequency we notice a reduction in roughness for all three materials: In the case of CVD SiC, there is a decrease in surface roughness from the short- to the long-dwell-time spot (see arrow 5). In the case of PCA, an increase in surface roughness from the short- to the long-dwell-time spot (see arrow 6) in a spatial-frequency range of 10^{-3} to 3.2×10^{-3} nm^{-1}, corresponding to features of the order of 1000 to 300 nm (comparable to the PCA grain size), is due to grain boundary highlighting by the MRF process, i.e., grain decoration.[43]

Conclusions

The response of three hard optical ceramics to deterministic microgrinding has been studied. Grinding experiments showed that grinding-induced surface roughness decreased with a decreasing size in the diamond abrasive used. Microgrinding with a rough tool involved fracture, leading to p–v surface roughness in the range of 14.5 to 4 μm (1.4- to 0.1-μm rms). Using high-magnification SEM images, we found that the deformed layer induced by grinding covered the actual damage depth/SSD.

We have demonstrated that an MRF spot can be placed on ground surfaces of hard ceramics without introducing additional damage, and that the spot can be used to estimate the induced SSD depth from microgrinding. For initially rough and medium surfaces, SSD depth is ~11 μm (ALON), ~1.7 μm (CVD SiC), and ~9 μm (PCA), corresponding to initial p–v surface roughness values of ~14.5 μm, ~3.7 μm, and ~9 μm, respectively. The evolution of surface roughness with the amount of material removed by the MRF process, as measured within the spot's deepest point of penetration (least roughness), can be divided into two stages: In the first stage the induced damaged layer and associated SSD from microgrinding are removed, reaching a low surface-roughness value. In the

second stage we observe interaction between the MRF process and the material's microstructure as MRF exposed the subsurface without introducing new damage. We showed that SSD depth can be estimated by using an optical profilometer–based measurement of the areal p–v surface microroughness of the as-ground surface. This provides an upper bound to the SSD value. SEM images confirmed these observations.

We also showed the development of the "MRF signature" on hard ceramics by computing PSD curves within the resolution capabilities of the interferometer and the AFM. By considering PSD data generated from profiles perpendicular to the MRF flow direction, we studied the residual grooving pattern of the MR fluid flow that represents the abrasive/surface interactions. Additional work is still needed, however, to characterize MR fluid particles/surface (i.e., materials' microstructure) interactions parallel to the MR fluid flow direction.

The spotting technique is intended only as a diagnostic tool, by removing material from rough surfaces to expose the subsurface damage. It does not reflect on the true polishing capabilities with MRF technology for hard ceramics.

ACKNOWLEDGMENT

The authors thank A. Shorey (QED Technologies, Rochester, NY) for the use of the AFM and H. Romanosky (LLE) for MRF spot-taking. The authors acknowledge the Laboratory for Laser Energetics at the University of Rochester for its continuing support. One of the authors (S. N. Shafrir) is an LLE Horton Fellow. Research was sponsored by the U.S. Army Armament, Research, Development and Engineering Center (ARDED) and was accomplished under Cooperative Agreement No. W15QKN-06-R-0501 and the U.S. Department of Energy Office of Inertial Confinement Fusion under Cooperative Agreement No. DE-FC52-92SF19460, the University of Rochester, and the New York State Energy Research and Development Authority. The views and conclusions contained in this document are those of the authors and should not be interpreted as representing the official policies, either expressed or implied, of U.S. Army ARDEC or the U.S. Government. The support of DOE does not constitute an endorsement by DOE of the views expressed in this article. The U.S. Government is authorized to reproduce and distribute reprints for government purposes notwithstanding any copyright notation herein.

REFERENCES

1. L. Yin *et al.*, Wear **256**, 197 (2004).
2. S. Malkin and T. W. Hwang, CIRP Ann. **45**, 569 (1996).
3. B. Lin *et al.*, Key Eng. Mater. **202/203**, 121 (2001).
4. A. G. Evans and D. B. Marshall, in *Fundamentals of Friction and Wear of Materials*, edited by D. A. Rigney (American Society for Metals, Metals Park, OH, 1981), pp. 439–452.
5. J. A. Menapace *et al.*, in *Laser-Induced Damage in Optical Materials: 2005*, edited by G. J. Exarhos *et al.* (SPIE, Bellingham, WA, 2006), Vol. 5991, p. 599102.
6. J. C. Lambropoulos, S. D. Jacobs, and J. Ruckman, in *Finishing of Advanced Ceramics and Glasses*, edited by R. Sabia, V. A. Greenhut, and C. G. Pantano, Ceramic Transactions, Vol. 102 (The American Ceramic Society, Westerville, OH, 1999), pp. 113–128.
7. K. R. Fine *et al.*, in *Modeling, Simulation, and Verification of Space-Based Systems II*, edited by P. Motaghedi (SPIE, Bellingham, WA, 2005), Vol. 5799, pp. 105–110.
8. J. Wang and R. L. Maier, Appl. Opt. **45**, 5621 (2006).
9. P. E. Miller *et al.*, in *Laser-Induced Damage Optical Materials: 2005*, edited by G. J. Exarhos *et al.* (SPIE, Bellingham, WA, 2006), Vol. 5991, p. 599101.
10. W. Kanematsu, J. Am. Ceram. Soc. **89**, 2564 (2006).
11. B. Zhang and T. Howes, CIRP Ann. **43**, 305 (1994).
12. B. Zhang and T. D. Howes, CIRP Ann. **44**, 263 (1995).
13. J. A. Randi, J. C. Lambropoulos, and S. D. Jacobs, Appl. Opt. **44**, 2241 (2005).
14. H. H. K. Xu, S. Jahanmir, and Y. Wang, J. Am. Ceram. Soc. **78**, 881 (1995).
15. J. A. Menapace *et al.*, in *Laser-Induced Damage in Optical Materials: 2005*, edited by G. J. Exarhos *et al.* (SPIE, Bellingham, WA, 2006), Vol. 5991, p. 599103.
16. F. W. Preston, Trans. Opt. Soc. **XXIII**, 141 (1921–22).
17. F. K. Aleinikov, Sov. Phys.-Tech. Phys. **2**, 505 (1957).
18. P. P. Hed and D. F. Edwards, Appl. Opt. **26**, 4677 (1987).
19. J. C. Lambropoulos, Y. Li, P. D. Funkenbusch, and J. L. Ruckman, in *Optical Manufacturing and Testing III*, edited by H. P. Stahl (SPIE, Bellingham, WA, 1999), Vol. 3782, pp. 41–50.
20. S. N. Shafrir, J. Lambropoulos, and S. D. Jacobs, Precision Engineering **31**, 83 (2007).
21. S. N. Shafrir, J. C. Lambropoulos, and S. D. Jacobs, "Technical Note: Toward Magnetorheological Finishing of Magnetic Materials," to be published in the Journal of Manufacturing Science and Engineering.
22. J. C. Lambropoulos, in *Optical Fabrication and Testing*, Vol. 42, 2000 OSA Technical Digest Series (Optical Society of America, Washington, DC, 2000), pp. 17–18.
23. A. G. Evans, in *Fracture Mechanics Applied to Brittle Materials*, edited by S. W. Freiman (American Society for Testing and Materials, Philadelphia, 1979), Vol. ASTM STP 678, Part 2, pp. 112–135.
24. D. Halliday, R. Resnick, and J. Walker, *Fundamentals of Physics*, 5th ed. (Wiley, New York, 1997).
25. SX 50 CNC deterministic microgrinding machine, OptiPro Systems, Ontario, NY 14519.

26. SX 150 CNC deterministic microgrinding machine, OptiPro Systems, Ontario, NY 14519.

27. Opticut GPM 5% in water, pH 9-10, Lighthouse Lubricant Solutions, LLC, Overland Park, KS 66282.

28. S. D. Jacobs, H. M. Pollicove, W. I. Kordonski, and D. Golini, in *International Conference on Precision Engineering*, ICPE '97 (ICPE, Taipei, Taiwan, 1997), pp. 685–690.

29. A. B. Shorey, S. D. Jacobs, W. I. Kordonski, and R. F. Gans, Appl. Opt. **40**, 20 (2001).

30. Q22-Y, QED Technologies, LLC, Rochester, NY 14607.

31. D10 MR fluid, QED Technologies, LLC, Rochester, NY 14607.

32. TalySurf 2 PGI profilometer, Taylor Hobson, Inc., Rolling Meadows, IL 60008-4231.

33. NewView™ 5000 noncontact profilometer, Zygo Corporation, Middlefield, CT 06455.

34. LEO 982 FE SEM, Nano Technology Systems Division, Carl Zeiss NTS GmbH, A Carl Zeiss SMT AG Company, 73447 Oberkochen, Germany.

35. Dimension 3100S-1 AFM, Digital Instruments/Veeco Metrology Dimension 3100S-1 Atomic Force Microscope, Veeco Instruments, Inc., Woodbury, NY 11797-2902.

36. Light Microscope, Leica Microsystems Inc., Bannockburn, IL 60015.

37. S. N. Shafrir, "Surface Finish and Subsurface Damage in Polycrystalline Optical Materials," Ph.D. thesis, University of Rochester, 2007.

38. S. R. Arrasmith, I. A. Kozhinova, L. L. Gregg, A. B. Shorey, H. J. Romanofsky, S. D. Jacobs, D. Golini, W. I. Kordonski, S. J. Hogan, and P. Dumas, in *Optical Manufacturing and Testing III*, edited by H. P. Stahl (SPIE, Bellingham, WA, 1999), Vol. 3782, pp. 92–100.

39. J. E. DeGroote, A. E. Marino, K. E. Spencer, and S. D. Jacobs, in *Optifab 2005* (SPIE, Bellingham, WA, 2005), Vol. TD03, pp. 134–138.

40. E. Marx *et al.*, J. Vac. Sci. Technol. B **20**, 31 (2002).

41. A. Duparré *et al.*, Appl. Opt. **41**, 154 (2002).

42. C. J. Walsh, A. J. Leistner, and B. F. Oreb, Appl. Opt. **38**, 4790 (1999).

43. L. L. Gregg, A. E. Marino, J. C. Hayes, and S. D. Jacobs, in *Optical Manufacturing and Testing V*, edited by H. P. Stahl (SPIE, Bellingham, WA, 2004), Vol. 5180, pp. 47–54.